Meteorol. Z. (Contrib. Atm. Sci.), Vol. **31**, No. 1, 69–86 (published online December 10, 2021)

Multi-year cloud and precipitation statistics observed with remote sensors at the high-altitude Environmental Research Station Schneefernerhaus in the German Alps

Stefan Kneifel[1*], Bernhard Pospichal[1], Leonie von Terzi[1], Tobias Zinner[2], Matjaž Puh[2], Martin Hagen[3], Bernhard Mayer[2], Ulrich Löhnert[1] and Susanne Crewell[1]

[1]Institut für Geophysik und Meteorologie, Universität zu Köln, Köln, Germany
[2]Meteorologisches Institut, Ludwig-Maximilians-Universität, München, Germany
[3]Institut für Physik der Atmosphäre, Deutsches Zentrum für Luft und Raumfahrt, Oberpfaffenhofen, Germany

(Manuscript received June 8, 2021; in revised form September 23, 2021; accepted September 27, 2021)

Abstract

Clouds and precipitation over mountainous terrain are a challenge for models and observations alike. In this study, we exploit a unique, nearly one decade long dataset of collocated microwave radiometer, radar, ceilometer, and auxiliary observations collected at the Environmental Research Station Schneefernerhaus (UFS). Located at 2650 m a.s.l. just 300 m below the summit of Zugspitze, Germany's highest mountain, this dataset allows a combined view on water vapor, clouds, and precipitation. Annual and diurnal cycles of water vapor, cloud liquid water, cloud ice, rainfall, and snowfall rate are investigated. Strong diurnal cycles during summer in several observables indicate a strong coupling with the surface and convective transport of air from the surrounding valleys to the level of UFS resulting in maximum amounts in integrated water vapor (IWV), cloud liquid water path (LWP) and rain during the afternoon. In contrast, no diurnal cycle is found during winter, which points to the predominance of advection of cloud systems associated with large scale dynamics during winter. Daily precipitation estimates for snowfall and rainfall derived from a vertically pointing, low-cost micro rain radar (MRR) are found to be in good agreement with manual observations from the German Weather Service at the summit. Exploiting the synergy of MRR and microwave radiometer measurements revealed that almost 90 % of the snow clouds contained significant amounts of super-cooled LWP but only a weak correlation between snowfall rate and LWP is found. The still growing data set at this very particular location, also in combination with further observations, such as trace gases and aerosols, has a unique potential for many applications, e.g. to investigate cloud processes, evaluate high resolution models, and to validate satellite products.

Keywords: Mountainous clouds and precipitation, Water Vapor, Liquid water path, Snowfall, Schneefernerhaus

1 Introduction

Clouds and precipitation are a central component of the hydrological cycle. In particular, mountainous regions store large amounts of water in form of snow, which makes them essential suppliers for drinking water and for agriculture in many regions (Viviroli et al., 2003). Mountains also actively interact with clouds and precipitation in a complex way (Dmowska and Holton, 1992). Examples for this interaction are clouds induced by mountain gravity waves (Carslaw et al., 1998), initiation of convection (Wulfmeyer et al., 2011), Lee wave and Banner clouds (Wirth et al., 2012; Schween et al., 2007), but also orographic blocking and enhancement of precipitation (Zängl, 2008; Rotunno and Houze, 2007; Houze Jr., 2012). With increasing resolution in numerical weather prediction but also in regional reanalysis products (e.g., Bollmeyer et al., 2015), the correct representation of these processes becomes an increasing challenge. Thus, there is a strong need for comprehensive observational datasets from mountainous regions for model evaluation and further development (Lundquist et al., 2019).

In the Alps, a relatively dense network of surface rain gauges provides a long-term record of daily precipitation accumulation, which allows to analyze the spatial variability of surface precipitation as well as its changes over climatological time scales (Isotta et al., 2014). Based on this dataset, Napoli et al. (2019) found that orographically influenced precipitation patterns in the Alpine region are particularly sensitive to global warming and anthropogenic forcing. To better understand and subsequently predict the complex dynamical and microphysical processes driving precipitation variability, high resolution measurements of variables involved in the water cycle are needed. For this, multiple sensors and observing methods (remote sensing, in-situ) need to be combined which is often only possible to realize during dedicated measurement campaigns (Grazi-

*Corresponding author: Stefan Kneifel, University of Cologne, Pohligstr. 3, 50969 Köln, Germany, e-mail: skneifel@meteo.uni-koeln.de

DOI 10.1127/metz/2021/1099

Gebrüder Borntraeger Science Publishers, Stuttgart, www.borntraeger-cramer.com

oli et al., 2015; Ramelli et al., 2021). Although specific processes, such as seeder-feeder processes (Ramelli et al., 2021) or turbulence induced riming (Grazioli et al., 2015) can be studied in detail with such datasets, the analysis is often limited to certain weather situations.

Classical long-term observations by satellite and ground-based scanning weather radars are prone to several uncertainties in alpine regions. Weather radar suffers from blocking of the radar beam by orography and clutter (Germann et al., 2006). Reflection from non-meteorological targets is also problematic for the vertical pointing Cloud Profiling Radar on-board the CloudSat satellite (Stephens et al., 2018). Especially in complex terrain, the strong surface reflection leads to a so-called radar blind zone of ca. 1500 m, Kulie and Bennartz (2009). Several studies revealed that microphysical processes in these lowest layers can systematically affect the surface precipitation rate (Maahn et al., 2014; Durán-Alarcón et al., 2019). Passive microwave satellite instruments, which are often used to infer properties of clouds and precipitation from space, are difficult to interpret due to their large footprint averaging over the highly heterogeneous surface. Therefore, space-borne observations are only of very limited use for investigating cloud processes in complex terrain.

Ground-based remote sensing sites with vertical profiling capabilities can to some extent fill this gap left by satellite and conventional weather radar observations. The long-term operation of a suite of remote sensing instruments and their synergistic analysis can provide important insights into atmospheric processes as demonstrated by the success of the Atmospheric Radiation Measurement (ARM) program and the European Cloudnet project (Haeffelin et al., 2016). For cloud and precipitation studies these stations combine among other instruments cloud radar, lidar (ceilometer), and microwave radiometer (MWR). When pointing vertically upwards, clouds and precipitation can be observed much closer to the surface. Such observations can be used to evaluate satellite products (Maahn et al., 2014), but also to better understand cloud processes associated with the lowest few hundred meters of the atmosphere, which are usually most affected by the orography.

Today not more than thirty of such cloud observing stations are continuously operating. To our best knowledge, only the Environmental Research Station Schneefernerhaus (UFS) currently provides multi-year observations from a high-altitude site. Only during a short campaign, ARM operated a mobile station in the Rocky Mountains (Marchand et al., 2013). Mountain stations also have a long history for trace gas measurements since they are often located above the mixing layer and can probe background conditions. Many of them (including the UFS) are organized in the Global Atmospheric Watch (GAW) programm of the World Meteorological Organization (Schultz et al., 2015).

Since 2006, the excellent infrastructure at UFS has been exploited for cloud and precipitation observations by combining MWRs, cloud and precipitation radars, and a lidar ceilometer. To the authors' knowledge, this dataset is the only one available for a ground-based site at this elevation and for a multi-year time period. The UFS (47.42° N, 10.97° E, 2650 m a.s.l.) is located in the Wetterstein mountain massif at the southern flank of Mount Zugspitze, 310 m below its summit. Sitting in the northern part of the Alps, UFS experiences intense precipitation events, which are often influenced by orographic precipitation enhancement caused by air masses advected from the north and north-west especially during wintertime (Wastl and Zängl, 2007; Wastl and Zängl, 2008). The average annual precipitation amount of ca. 2090 mm (average for 1991–2000, Wastl and Zängl (2008) and references therein) is typical for the general northern alpine region (Isotta et al., 2014). The nearby Zugspitze summit also hosts one of Germany's oldest mountain weather observatories with continuous manual observations starting in 1900 (Lüdecke, 2000).

At the UFS, the first MWRs were installed in 2006. These instruments cover a frequency range from 22 up to 150 GHz and provide information about water vapor and temperature profile, as well as columnar liquid water path (LWP). The two MWRs were complemented in 2008 by a vertically pointing Ka-band (35.5 GHz) Doppler cloud radar (Görsdorf et al., 2015) as part of the TOSCA campaign (Towards an Optimal estimation based Snowfall Characterization Algorithm; Löhnert et al., 2011). In 2011, the cloud radar was permanently installed at UFS. A low-power Doppler radar system, the Micro Rain Radar (MRR, Peters et al, 2002) operating at 24 GHz, was installed in 2008. Its robustness and small size makes it a very valuable instrument for this mountain station with harsh weather conditions. Although the MRR was initially designed for rain, the parallel observations with a cloud radar at the UFS allowed to develop new MRR data processing algorithms for snowfall (Kneifel et al., 2011a; Maahn and Kollias, 2012).

A number of studies already explored the particular value of multi-year observations of combined active and passive remote sensor observations at UFS. Scattering signals of snowflakes, which are useful to improve snowfall retrievals, have been detected for the first time in ground-based MWR observations collected at UFS by Kneifel et al. (2011a). Xie et al. (2012) further explored this effect and could show a general preferential horizontal orientation of snowflakes by investigating the polarimetric signature in the high frequency MWR channels and MRR radar reflectivities. The frequent occurrence of super-cooled liquid water (SLW) at UFS provided multi-year statistics for the development of improved absorption models for SLW, which are needed for global LWP retrievals and data assimilation (Kneifel et al., 2014; Turner et al., 2016; Rosenkranz, 2015; Lonitz and Geer, 2019). Cirrus clouds and their ice crystal properties above UFS were studied in Zinner et al. (2016) with passive remote sensors operating in the solar wavelength region. Long-term statistics of cloud and precipitation properties are also

Table 1: Overview of instruments, data products, and available time periods.

Instrument	Specification	Measured quantity	Retrieved products	Time period	Data availability
HATPRO	14 channel MWR, 22–31 GHz, 51–58 GHz	Brightness Temperatures	IWV, LWP, T and RH–profile	2006–now	80 %
CHM15Kx	Ceilometer (1064 nm)	Attenuated backscatter	Cloud base height	2010–now	90 %
MIRA36	Ka-band (35.5 GHz) vertically pointing Doppler radar	Doppler spectrum	Radar moments	2012–now	83 %
MRR1	Low-power, K-band (24.2 GHz), vertically pointing Doppler radar	Doppler spectrum	Radar moments (100 m vertical resolution)	2008–now	92 %
MRR2	Low-power, K-band (24.2 GHz), vertically pointing Doppler radar	Doppler spectrum	Radar moments (25 m vertical resolution)	2012–2015	91 %
PARSIVEL	Optical Disdrometer	Hydrometeor light extinction	Hydrometer type, size, velocity	2008–now	94 %

very valuable for planning of continuous observations or measurement campaigns at UFS, which require specific weather conditions (e.g., Witschas et al., 2012; Risius et al., 2015).

Starting with data back from beginning of 2012, the observations collected at UFS were integrated into Cloudnet, the cloud observation network of ACTRIS (Aerosol Clouds and Trace Gases Research Infrastructure, https://actris.eu/) in 2018 through funding within the HD(CP)^2 research initiative (High Definition Clouds and Precipitation for advancing Climate Prediction). MWR, radar, and ceilometer observations are used to produce cloud retrieval and classification products according to the Cloudnet standard (Illingworth et al., 2007). [1]

In this study, we utilize the multi-year dataset of remote sensing observations in order to obtain insights into the long-term variability of clouds and precipitation at a unique high-altitude location. The dataset, instrumentation, and methods are described in Section 2. The annual and diurnal variability derived from the combination of remote sensors and the Cloudnet algorithm are analyzed in Section 3. In Section 4, the daily accumulations of snowfall and rainfall derived from the MRR and the manual observations by the German Weather Service (DWD) are compared. As SLW is known to play a key role for snowfall, we also analyze the frequency of SLW during snowfall events at UFS by combining MRR and MWR observations. Finally, in Section 5, we contextualize the main findings of our study into current demands for weather and climate research and discuss future perspectives for observations at UFS.

2 Data and methods

The core instrumentation used for the analysis of cloud and precipitation properties consists of a MWR, a ceilometer, and vertically pointing radars. The key specifications of all instruments and their available data periods are summarized in Table 1. A more detailed description will be provided for the MWR and MRR because major parts of the analysis are based on those instruments. Ceilometer and cloud radar data are only used in this study as input for the Cloudnet algorithm.

2.1 Microwave Radiometer

The Humidity And Temperature PROfiler (HATPRO, Rose et al. (2005), Radiometer Physics GmbH) was installed at UFS in 2006. The measurements at 14 channels, 7 of them along the 22.235 GHz water vapor absorption line and additional 7 channels along the 60 GHz oxygen absorption complex allow to retrieve columnar integrated water vapor (IWV) and LWP in addition to temperature and humidity profiles. These atmospheric parameters are derived with multivariate linear regression as described in Löhnert and Crewell (2003) and are available with a temporal resolution of 1 s. The statistical retrieval was derived using 18 years (1992–2009) of high-resolution radio soundings from Payerne, Switzerland (ca. 300 km distance), using only altitudes starting at 2650 m in order to match the UFS altitude. Experiments using radio soundings from Munich did not show notable differences in the retrievals due to their similar climatic conditions and exclusion of the lower atmospheric layers. Taking into account uncertainties due to calibration offsets, channels drifts and retrieval uncertainty, we estimate the absolute accuracy of the derived IWV to be better than 0.5 kg m^{-2} and 20 g m^{-2} for LWP. HATPRO is able to measure LWP changes on the order of 5–10 g m^{-2} (Marke et al., 2016). In situations without any liquid clouds, the statistical retrieval produces LWP fluctuations (even negative LWP) around zero. In order to avoid biases in the statistics, we set the LWP to zero if the standard deviation of LWP over 20 minutes is below 1.5 g m^{-2}. Comparisons with ceilometer and infrared radiometers,

[1] Cloudnet products from UFS are freely available via https://cloudnet.fmi.fi/.

which are more sensitive to small LWP values, showed that this criterion is a reasonable choice. For the statistics of this study, we require the LWP to exceed 10 g m^{-2} to unambiguously detect the presence of cloud liquid water.

As liquid drops and melting snow on the radome of the instrument can deteriorate the measurements, HATPRO is equipped with a heated blower system. In addition, the status of the radome is under surveillance with a web-camera and a spotlight. Data quality is ensured by regular calibration with liquid nitrogen (every 6–12 months) and data consistency checks, which determine whether an observed spectral distribution of brightness temperatures is physically reasonable. Scattering effects by ice and snow particles in the atmosphere are generally negligible at the frequencies used by HATPRO (Kneifel et al., 2011b). For further analysis, all data were filtered by applying a spectral consistency retrieval to the observed brightness temperatures. In case of a wet radome, or other influences (e.g receiver instabilities or external radio sources), the measured spectrum does not agree with the modelled one, and hence these situations were flagged.

2.2 Cloudnet products

The Cloudnet algorithm (Illingworth et al., 2007) provides a classification of clouds and precipitation into several categories (e.g., cloud ice, rain or drizzle, liquid clouds, melting ice) on a vertical grid of 30 m and with a temporal resolution of 30 s. In order to apply the standardized algorithm, a combination of ceilometer, cloud radar, and MWR is required.

The ceilometer used for Cloudnet at UFS is of type CHM15Kx (manufactured by Lufft, Heese et al., 2010; Wiegner and Geiss, 2012), which is operated by the DWD and was installed in 2010 in less than 20 m distance to the MWR and the radars. It measures the backscatter profile from aerosols and hydrometeors and is sensitive to small amounts of cloud liquid water, even if embedded in optically thin ice clouds (Delanoë and Hogan, 2010). The Cloudnet algorithm uses it in combination with other remote sensors to identify aerosol layers, cloud base, and to distinguish clouds from insects and precipitation.

At the end of 2011, a Ka-band cloud radar (MIRA36 manufactured by Metek GmbH, Görsdorf et al. (2015)) was permanently installed at UFS, which completed the instrument suite needed for generating Cloudnet products. The MIRA36 is a powerful (25 kW peak power), zenith pointing cloud radar with high sensitivity to ice and liquid clouds up to 15 km range. MIRA36 records the full Doppler spectrum from which standard radar moments, such as equivalent reflectivity factor (Ze), mean Doppler velocity (MDV), spectrum width (SW), and skewness (Sk) are derived. Its receiver provides two polarizations (linear H/V), which allows to also derive the linear depolarization ratio (LDR). LDR is an important additional observable for Cloudnet in order to determine the melting layer and to detect the presence of insects. The lowest reliably usable range gate is at ca. 300 m above the radar.

Until present, an 8 year long Cloudnet dataset has been generated. Note that the time series contains several data gaps due to the necessary simultaneous availability of the three instruments. Overall, the data availability of the Cloudnet products is about 60 %, with multiple months missing in 2015, 2016 and 2019. As snow cover is largest during winter and early spring, sensors covered by snow as well as associated damages are causing the months of February and March to be under-represented as compared to the other months. We merged some of the Cloudnet classes into broader categories in order to simplify the following discussion. The various ice containing Cloudnet classes "ice", "ice and super-cooled droplets", "melting ice" are summarized into "cloud ice". The liquid precipitation classes "drizzle or rain" and "drizzle/rain and cloud droplets" are collected in a single "rain" category. Our categories "aerosols" and "insects" are identical with the original Cloudnet classes. If Cloudnet reports "aerosols and insects", those time periods are assigned to both categories. Several of the original classes as well as our categories will appear in each individual profile. For example, the same profile can contain aerosols at low levels and cloud ice at upper levels; then the profile will be assigned to both categories.

2.3 Micro Rain Radar

The UFS site is also equipped with a low-power (150 mW) frequency-modulated continuous wave (FMCW) Micro Rain Radar (MRR, Metek GmbH, Peters et al., 2002) operating at K-band (24.23 GHz). The MRR has been originally designed to observe rainfall, but has been found by several studies to be also usable for snowfall (Kneifel et al., 2011a; Maahn and Kollias, 2012; Souverijns et al., 2017). The MRR (MRR1) has been run with the default range resolution of 100 m which, together with the maximum number of 30 range gates, results in a maximum range of 3 km. A comparison of the different sensitivities of MRR and MIRA36 at UFS can be found in Kneifel et al. (2011a). A second MRR (MRR2) has been run at the UFS from 28 September 2012 until 13 August 2015 with a finer resolution of 25 m and a maximum total range of 750 m. All MRR raw data are routinely re-processed with the software tool Improtoo described in Maahn and Kollias (2012), which derives radar moments (Ze, MDV, SW) directly from the Doppler spectra and also applies post-processing steps which enhance the overall sensitivity of the MRR.

The MRR data have been checked for calibration offsets using the collocated PARSIVEL disdrometer (Löffler-Mang and Joss, 2000) observations similar to the approach described in Kneifel et al. (2011a), Dias Neto et al. (2019), and Myagkov et al. (2020).

Usually, the first 3–5 range gates of the MRR are not usable due to surface clutter or receiver saturation effects (Kneifel et al., 2011a) which results in a lowest usable range gate for the coarser resolved MRR1 of 500 m. We identified 30 rainfall cases in the time period 2013–2018 with sufficiently high melting layer and relatively stratiform rainfall. For those cases, we used the rain drop size distribution measured by the PARSIVEL and calculated the associated Ze values. The comparison revealed no significant calibration offset of MRR1 (the accuracy of this method can be assumed to be in the range of 2 dB). When comparing the MRR2 measurements with the simultaneous measurements of MRR1, we found a systematic underestimation of the Ze values measured by MRR2 of 3.5 dB. We assume that this difference is caused by a mis-calibration and corrected the MRR2 by this constant offset.

Although the MRR is a much less sensitive radar compared to the MIRA36, we perform our precipitation analysis with the MRR for two main reasons. First, the MRR has a small size (similar to a satellite TV antenna), a low-power consumption, and it is an extremely robust instrument. This makes it a favorable instrument to run in harsh and remote environments, where operation of a cloud radar might not be possible. Second, the possibility of the MRR to set a very fine range gate spacing, which results in a very low first usable range gate, is very advantageous for interpreting the MRR output as a disdrometer. It is expected that the limited sensitivity of the MRR will affect observations of very weak precipitation events (Kneifel et al., 2011a).

During the time period when the two MRRs were collecting data simultaneously, we analyzed the change of Ze in the lowest 500 m. For the fine-resolution MRR2, the reflectivities at 300 m (level of the summit station) are often found to significantly differ (in the range of 2–5 dB) from the lowest usable range gate (500 m) of MRR1. Changes of Ze in the lowest layers have been also frequently found at other sites (Maahn et al., 2014; Durán-Alarcón et al., 2019). In general, these gradients are found to vary strongly from case to case but frequently we find Ze to increase towards the ground. This leads to significant biases in the estimated snowfall accumulations. We speculate that several effects might be responsible for the Ze gradients. Turbulence generated by the mountain crest might enhance the frequency of particle collisions enhancing formation of aggregates. Enhanced turbulence might also generate super-cooled liquid which then can increases the particles' degree of riming as found in the Swiss Alps by Grazioli et al. (2015). For consistency with the comparison to the DWD observations at summit level, we decided to only use observations at 300 m range, although this limits the analysis to the shorter time period of the higher resolved MRR2.

For the analysis of precipitation, the data from MRR2, MWR, as well as the 2 m air temperature data measured by the DWD at the UFS have been averaged onto a common five minute time grid. In order to separate rainfall from snowfall cases, we use a simple temperature threshold, which is similar to the approach used in precipitation retrievals from satellites (Smalley et al., 2014). We use the 2 m air temperature measured at UFS in order to infer the approximate temperature at 300 m assuming a constant lapse rate of 0.006 K m^{-1}. We classify the Ze measurements as belonging to rainfall, if the temperature at 300 m is larger than 2 °C. If the temperature is lower than −2 °C, we assign the Ze to snowfall. Temperatures within these limits are assumed to be affected by melting ice particles and are discarded. The final snowfall rate (SR) and rainfall rate (RR) are derived from the MRR2 observations applying previously published Ze-SR and Ze-RR relations (details described in Appendix 1).

3 Annual and diurnal cycle of water vapor, clouds, and precipitation

The unique multi-year record of remote sensing observations at UFS provides the opportunity to derive statistics of clouds and precipitation at UFS including a wide range of parameters. In contrast to space-borne observations, ground-based datasets have the advantage of being unaffected by averaging effects over a satellite sensor footprint or commonly enhanced retrieval uncertainties due to heterogeneous surface properties and complex terrain.

From previous studies (Wastl and Zängl, 2007; Wastl and Zängl, 2008; Sigmund et al., 2019) we expect to find distinct seasonal differences in cloud and precipitation properties, especially between summer and winter. Those differences are not only related to the different temperature conditions but also due to different cloud formation mechanisms and air mass advection. During winter, ice and mixed-phase clouds are typically advected over the Alps by synoptic-scale systems. In high-pressure conditions, the high altitude regions are often in clear sky conditions, while the valleys are commonly covered by long-lasting stratus decks at the top of the mixing layer (Wastl and Zängl, 2007; Wastl and Zängl, 2008). During summer months, the orography often initiates or amplifies convection. As a result, the mixing layer extends frequently up to and above the altitude of UFS, which occasionally results in the formation of convective clouds and precipitation (Lugauer and Winkler, 2005). We expect those well-known mechanisms to cause distinct differences in the annual and diurnal cycle of several cloud and precipitation variables, which we will analyze in the following in more detail.

3.1 Annual cycle

Before looking at specific cloud and precipitation related variables, the annual cycle of temperature and absolute humidity measured at the UFS by DWD is shown in Figure 1a–b. The monthly mean temperature at UFS peaks at 7 °C in August and reaches its minimum of −8 °C

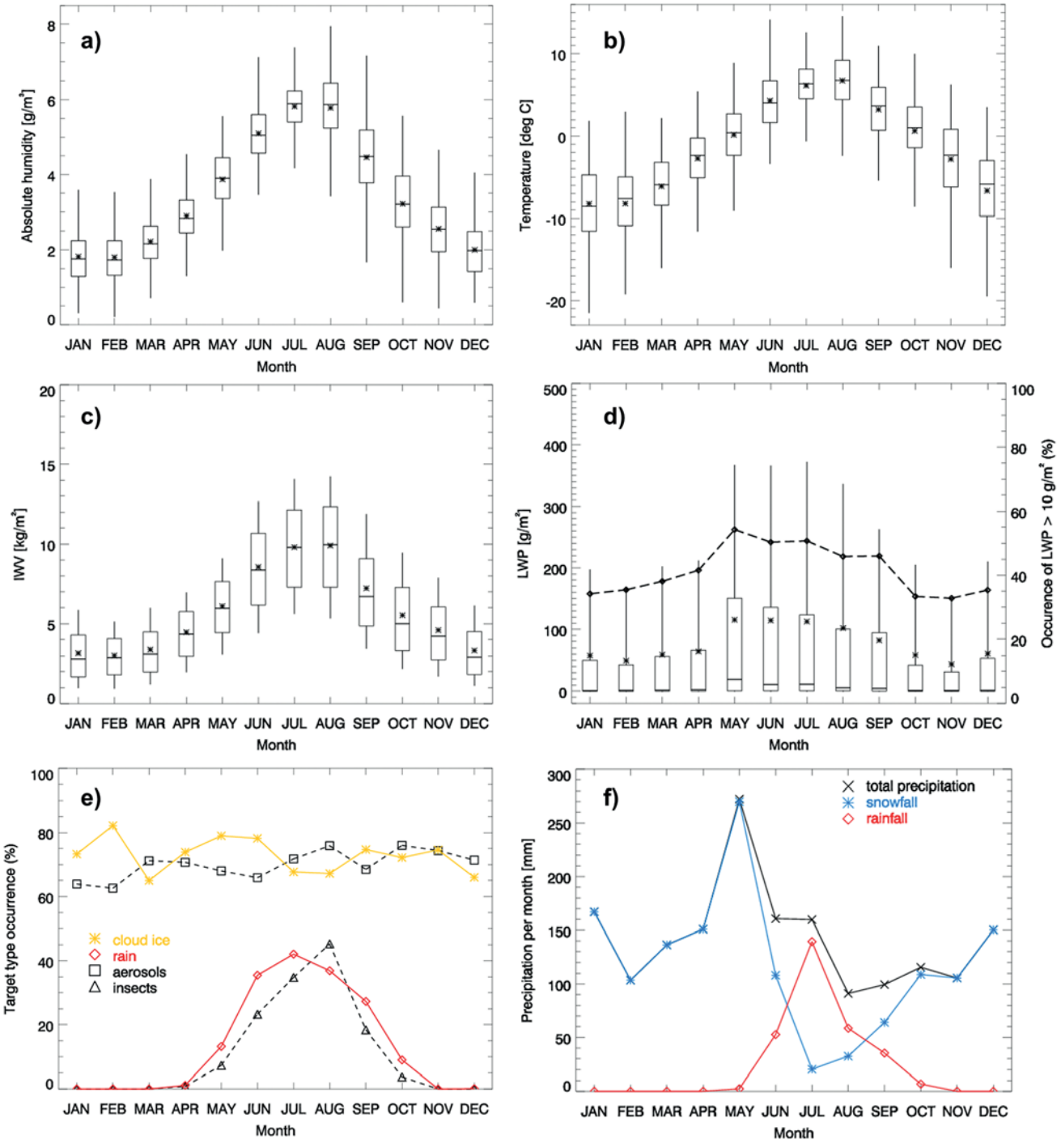

Figure 1: Annual cycle of a) absolute humidity and b) surface temperature measured at the UFS by DWD (time period 2008–2020). Vertically integrated amounts of c) water vapor (IWV) and d) liquid water path (LWP) above the UFS have been derived from almost 10 years of HATPRO observations. The dashed line in d) denotes the frequency of occurrence of LWP exceeding 10 g m^{-2} (right y-axis). In a)–d) the mean is shown as asterisk, the median is plotted as line inside the box of the 25th and 75th percentile. The whiskers denote the 10th and 90th percentiles. Occurrence frequency of ice (yellow), rainfall (red), aerosols (squares), and insects (triangles) present in the entire vertical column are shown in e) based on the Cloudnet classification algorithm. Note that also multiple Cloudnet classes (e.g., ice and snow above rainfall) or several cloud layers might be present in the column at the same time. The monthly accumulated rain (red) and snow (blue), as well as the total accumulation as derived with MRR2 are shown in f). Note that the statistics are derived from observational time periods with different duration (see Table 1). Especially the MRR2 data (panel f) are only available from 2012–2015.

in January. Absolute humidity values similarly show a maximum in the mean values of 6 g m^{-3} in July and the driest period with values of 1.8 g m^{-3} in February. Such annual cycles are typical for a mid-latitude alpine climate. We included them here, in order to provide context for the following discussion of annual variability of cloud and precipitation properties.

To illustrate the annual cycle of clouds and precipitation, a number of selected variables derived from the combination of radar, ceilometer, and MWR is shown in Figure 1c–f. It should be noted that the length of the data records varies for the different sensors (Table 1). Given the strong year to year variability, especially the shorter (3 years) period of MRR2 observations (Figure 1f) should be interpreted with care. The seasonal variability of columnar amounts of water vapor (IWV) and liquid water (LWP) above the UFS (Figure 1c–d) are based on more than a decade of HATPRO observation (Table 1). IWV and LWP statistics are derived for all weather conditions except for heavy rainfall events due to possible contamination of the MWR radome with liquid water.

The annual cycle of columnar water vapor (Figure 1c) is similar to the annual cycle of absolute humidity (Figure 1a) and shows the lowest mean IWV of around 3 kg m^{-2} during winter and the largest mean IWV values of 10 kg m^{-2} during summer. Also the spread of IWV is found to be much larger in summer with its 10th/90th percentile ranging from 6 to almost 15 kg m^{-2}. The differences of the annual cycle between individual years are found to be relatively small (not shown). During summer, we expect that humidity from the surrounding valleys lifted up to the altitude of the UFS by convective processes is contributing to the measured IWV. This assumption is corroborated by the analysis of air mass origins at UFS presented in Sigmund et al. (2019). In winter, the UFS is typically within the free troposphere as indicated by the generally low values of IWV. Occasionally, the IWV can drop down to 0.2 kg m^{-2} during cold and clear-sky winter days. Throughout the year, the IWV values observed at UFS are by a factor of 2–3 smaller as compared to a lowland site, for example, the Jülich ObservatorY for Cloud Evolution (JOYCE, 111 m a.s.l., Löhnert et al. (2015)) 40 km west of Cologne.

A distinct annual cycle is also found for the LWP (Figure 1d). The monthly mean LWP values vary between 50 and 130 g m^{-2} throughout the year, whereby LWP during summer is almost a factor of two larger both for the 90th percentiles and the mean. The annual mean LWP of 73 g m^{-2} falls within the range of annual, zonal mean LWP values (70–90 g m^{-2}) derived from satellite sensors for the UFS latitude (Lohmann and Neubauer, 2018). This agreement is somewhat surprising considering the special location of UFS. The relatively large uncertainty range found in space-borne LWP observations also emphasizes again the importance of long-term ground-based LWP datasets as they can provide LWP time series with high accuracy even in complex terrain. The larger mean and extreme LWP values at UFS during summer coincide with the much higher occurrence of clouds that form due to local convection over the UFS in summer as opposed to winter. Moreover, rainfall events during summer are more frequent because of temperatures above freezing, as shown in Figure 1b, e. During winter, the LWP is mainly present as SLW embedded in mixed-phase clouds (see also Löhnert et al., 2011). Both aspects will be investigated in more detail later when looking at the diurnal cycle and the frequency of SLW during snowfall events captured by the MRR2.

Particular differences are found when analyzing the annual cycle of different cloud types. Ice and mixed-phase clouds (which are summarized in the ice cloud category in Figure 1e) occur with a relatively weak annual cycle ranging between 65 and 85 % throughout the year. It should be noted that this category also includes precipitating cases, for example, summer convection events with ice particles in the upper cloud part and rainfall below. In contrast to the ice cloud category, the frequency of liquid containing clouds shown in Figure 1d (right y-axis), ranges from 30 to 55 % with a broad peak during the warmer seasons. The frequency of liquid containing clouds has been derived from the HATPRO observations applying a simple LWP threshold of 10 g m^{-2} (see also Section 2). As the HATPRO measurements are unaffected by ice particles, this cloud liquid frequency includes pure liquid clouds as well as mixed-phase clouds. The high frequency of liquid water containing clouds above the UFS (roughly 45 % throughout the year) together with the high frequency of ice and mixed-phase clouds (ca. 70 %) indicates that most clouds at UFS are either mixed-phase or composed by multiple layers of liquid and ice clouds.

In addition to the classification of clouds, Cloudnet also provides information on the presence of aerosols and insects. The aerosol detection is limited by the sensitivity of the used ceilometer as well as the presence of clouds; insects can be well identified due to their strong depolarization of the emitted horizontally polarized radar signals. It can be clearly seen in Figure 1e that the aerosols are detected in 60–80 % of the time with very weak seasonal variability. A completely different behaviour is found for insects, whose presence is clearly limited to the months with mean temperatures larger than 0 °C (May–October, see Figure 1b). Not only are positive temperatures required for the insects to fly but also the lifting of insects from the valley to the UFS altitude is enhanced during summer probably due to strong updrafts along the mountain slopes (Sigmund et al., 2019).

Rainfall is only observed at UFS between April and November as revealed by the independent statistics of Cloudnet (Figure 1e) and the MRR2 (Figure 1f). The maximum frequency of rainfall (ca. 50 %) as well as the average monthly accumulation (ca. 150 mm) occur both in July. During this month, almost all precipitation falls as rain, which is simply explained by the fact that

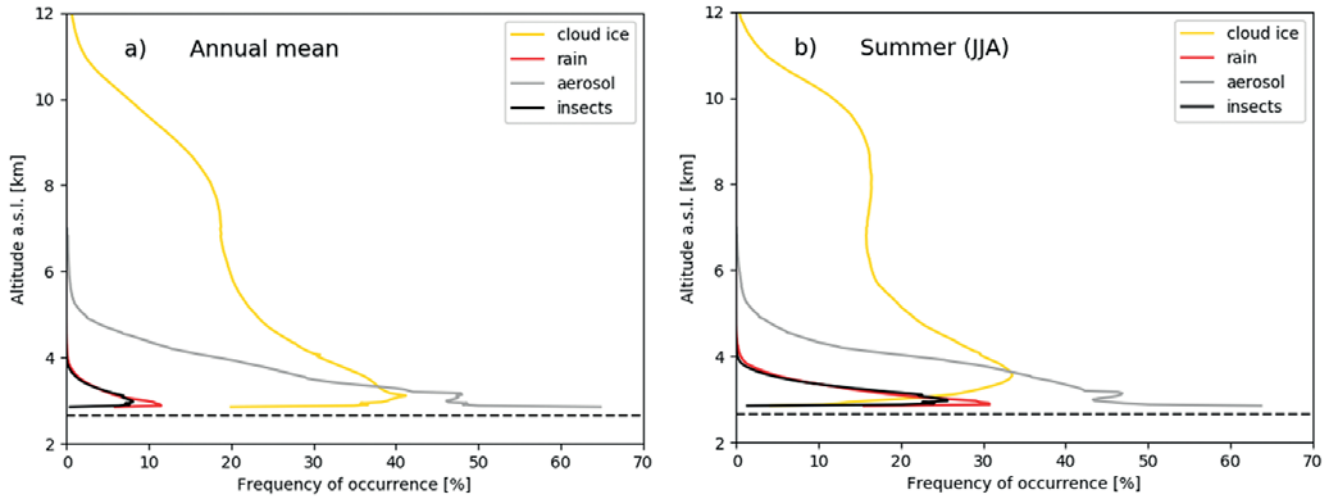

Figure 2: Vertical profiles of the frequency of occurrence of the different cloud and precipitation categories derived from the original Cloudnet classification (for details see Section 2.2): ice and mixed-phase clouds (yellow), rain and drizzle (red), aerosols (grey), and insects (black). Annual mean profiles are shown in a) and mean profiles for summer months (JJA) in b). The horizontal dashed black line denotes the altitude of the UFS (2650 m a.s.l.).

90 % of the occurring temperatures at the UFS are found to be larger than 0 °C (Figure 1b). The largest amount of monthly precipitation during the three years time period covered by the MRR2 data occurs in May with 270 mm falling entirely as snow. A more detailed investigation of the statistics of rainfall accumulations and typical snowfall and rainfall rates for different seasons will be provided in Section 4.

The combination of passive and active remote sensors at UFS allows to investigate also the vertical distribution of clouds and precipitation (Figure 2). According to the categories defined in Section 2.2, a very prominent feature is the bi-modal distribution of ice and mixed-phase clouds. The ice category is found most frequently (more than 40 %) throughout the year within the first 1–2 km above UFS (Figure 2a). A second maximum of 20 % for this category is present at around 8 km (a.s.l.). Both maxima are found elevated by roughly 1 km during summer months (Figure 2b). Overall the observed bi-modal signature is in agreement with cloud radar derived statistics of vertical cloud occurrence frequency from lower altitude mid-latitude sites (e.g., Protat et al., 2006).

Rainfall is only found during summer up to altitudes of 4 km (a.s.l.). Interestingly, the height dependence of the occurrence frequency of insects is very similar to rain, probably due to the limitations of insects flying only at temperatures larger than 0 °C. Throughout the year, the ceilometer is able to detect aerosols up to 6 km (a.s.l.) with slightly thicker layers during summer.

3.2 Diurnal cycle

The seasonal differences in cloud and precipitation regimes, which we presented in the previous section, are also expected to manifest themselves in distinctly different diurnal cycles due to their different generation mechanisms. We will investigate in the following the diurnal variability of water vapor, cloud and precipitation at the UFS for different seasons.

The seasonally dependent coupling of the UFS to lower and more humid atmospheric layers can be observed in the diurnal cycle of IWV (Figure 3a). As the IWV itself shows a very large day-to-day variability, we calculate the relative anomaly of the IWV from the daily mean. No diurnal cycle can be found during winter (DJF) when the UFS can be expected to be mostly within the free troposphere and local moisture fluxes are relatively small. A maximum of IWV anomalies (up to 5 %) becomes visible around 14–15 UTC during spring (MAM) and autumn (SON). As expected, the largest anomalies are found during summer (JJA) with deviations from the mean up to 11 % at 14–15 UTC and a smaller minimum of −8 % at 7–8 UTC. Also the most extreme absolute IWV anomalies are found during summer and can reach up to ± 10 kg m^{-2} (for example on 30th June 2019 or 17th July 2019). A pronounced seasonally dependent cycle of IWV was also found in the study by Steinke et al. (2019) where IWV from Global Positioning System (GPS) data was derived for a large number of stations across Germany. Interestingly, they found the largest IWV anomaly to appear slightly later at 16–18 UTC with only 50 % of the amplitude observed at UFS. The larger magnitude of IWV deviation at UFS seems to be corroborated by the findings of previous studies (Diedrich et al., 2016; Adler et al., 2016; Steinke et al., 2019) which showed that relative diurnal IWV anomalies are in general increasing with higher station altitudes.

There might be various reasons for the earlier IWV maximum and the observed larger diurnal cycle at UFS

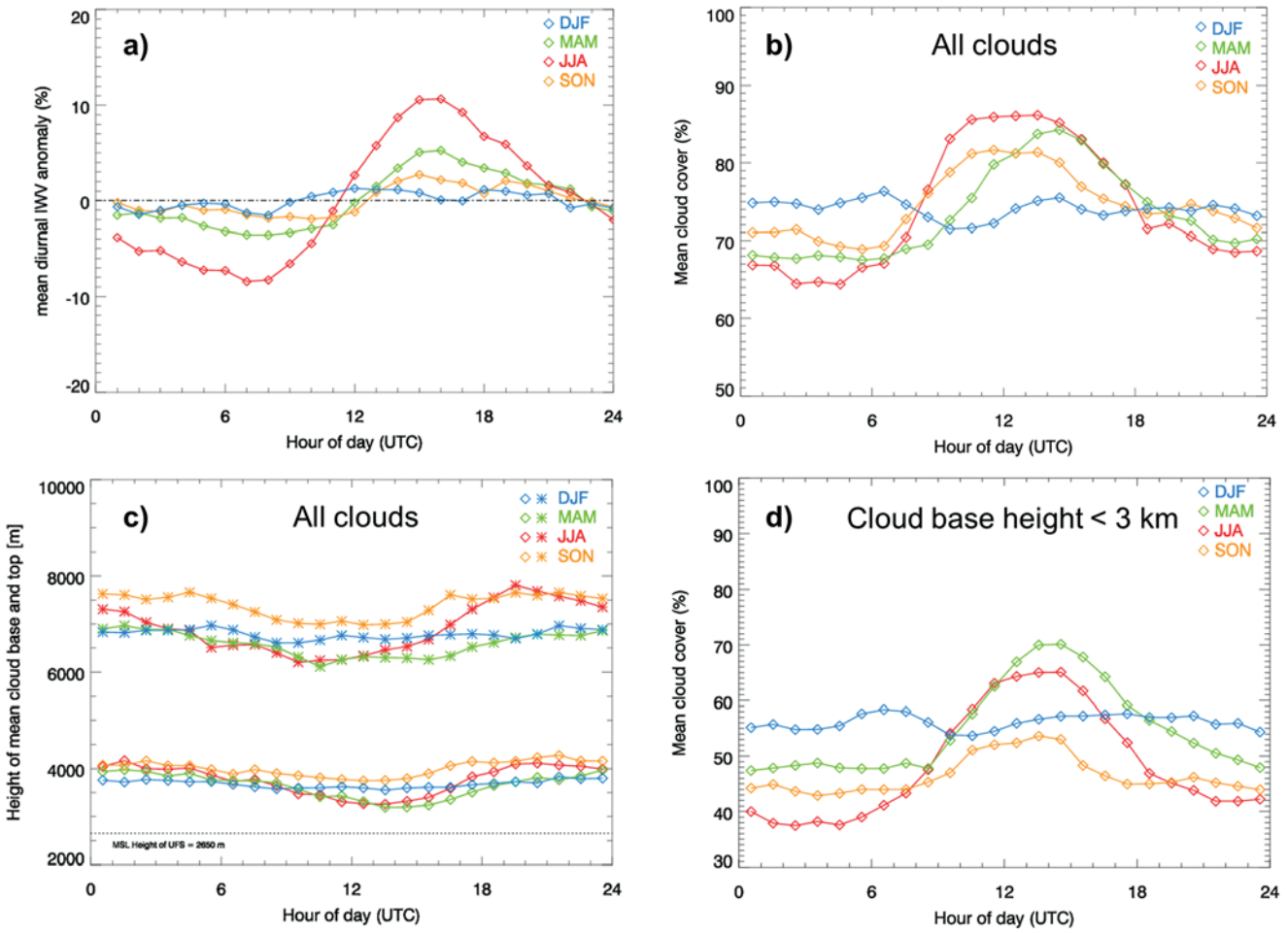

Figure 3: a) Relative anomaly of IWV from the daily mean for different seasons. b) Diurnal cycle of mean cloud cover and d) mean cloud cover for all clouds with cloud base heights below 3 km a.s.l. (close to altitude of Zugspitze summit). c) Height (a.s.l.) of lowest cloud base (diamond) and highest cloud top (asterisk) at UFS averaged for different seasons (colored). The black dashed line in c) denotes the altitude of UFS (2650 m a.s.l.). In b)–d) all cloud and precipitation categories are used for detecting presence of a cloud. A cloud layer is identified if its thickness is exceeding 70 m (corresponding to approximately two cloud radar range gates) and a profile is identified as cloudy, if any layer is present. The number of cloudy profiles (30 s time resolution) is normalized by the total number of measured profiles and averaged over one hour.

which we can only partly answer with our dataset. However, similar to many mountainous regions, a distinct thermal circulation pattern can be observed especially during summer in the northern Alpine region where the UFS is located (Lugauer and Winkler, 2005). The different heating of the mountain slopes compared to the foreland leads to a pronounced circulation pattern ("alpine pumping"). The maximum of the vertical transport of pollutants and moisture up to altitudes of UFS is commonly reached in the early afternoon. Once this thermal circulation declines, the IWV is expected to decrease as well due to a lack of moisture supply from the valley. The exact time when the thermal circulation decreases might be very dependent on the weather situation and season. However, it is likely that it happens earlier than the decrease of moisture fluxes in the lower altitude regions. Another reason could be that local sources of latent and sensible heat in the high Alpine region decrease earlier simply because the sun becomes blocked by the surrounding mountains. Another mechanism which might impact the daily IWV evolution is advective venting of moisture, i.e. the downstream transport of moisture with the mean wind found by Adler et al. (2016) for the island of Corsica. Finally, the larger magnitude of the diurnal IWV deviations might be connected to the fact that the average IWV generally decreases with higher altitudes. An identical absolute IWV variation would therefore automatically cause a larger relative IWV anomaly at higher elevations.

The diurnal cycle of total cloud cover for different seasons (Figure 3b) reveals almost no diurnal variability during winter but an increasing diurnal cycle for warmer seasons with a maximum during summer. The fact, that cloud cover in summer shows its peak during daytime fits well to the assumed predominance of convectively induced clouds during the warmer seasons.

The general high cloud cover of 65 to 85 % throughout the year for UFS agrees very well with average total cloud cover estimates of 70–80 % for this region derived from multi-year satellite observations (Kästner and Kriebel, 2001). Also the diurnal cycle of cloud bases and cloud tops (Figure 3c) shows again almost no variability in winter and a more pronounced pattern for the warmer seasons. Similar seasonal dependencies are found in a recent study by Risius et al. (2015), where the relative humidity measured at UFS was used to determine whether the UFS is located inside clouds. Throughout the year, the probability that UFS is inside clouds ranges from 15 to 30 % with the maximum found in July.

Interesting additional insights into the presence of different cloud types across different seasons can also be gained if we restrict the maximum cloud base height to 3 km a.s.l. (Figure 3d) which is close to the height of the Zugspitze summit (2960 m a.s.l.). We find again no diurnal cycle in winter but we can see that 55 % of the total 75 % cloud cover in winter (Figure 3b) is related to clouds below the altitude of the summit. Interestingly, we find the increase in the morning (8–12 UTC) during spring and summer to be very similar for the low-base clouds in contrast to the delayed increase seen for all clouds in spring (Figure 3b). Convective clouds seem to build up with low cloud bases both in spring and summer, which could be related to the overall similar insolation for example in May and July. However, in summer, the bases of the convective clouds appear to further rise upward probably due to an increasing lifting condensation level. We suspect that the lower frequency of low-base clouds in autumn is related to decreasing insolation and generally more stably stratified lower atmosphere.

For most variables, such as IWV, LWP, precipitation rate, or Cloudnet categories, we could not find any distinct diurnal cycle during winter. We interpret this absence of diurnal variability as an indication that clouds and precipitation are predominantly advected by large scale systems. Therefore, we focus our analysis in the following on the diurnal cycle in summer (JJA) and combine the various observables from the remote sensing suite into a consistent interpretation.

In the morning at around 7–8 UTC, we expect first smaller convective clouds to develop and later deepening due to the increasing thermal circulation from the valley and local fluxes of sensible and latent heat. This picture seems to be confirmed by the strongly increasing total cloud cover (Figure 3b, d) during morning hours. Interestingly, also the frequency and amount of rainfall (Figure 4d, e) increases already in the morning. The simultaneous increase of ice clouds (Figure 4d), however, needs to be interpreted with care as the presence of a convective cloud with an ice phase is also assigned to the cloud ice category.

During noon and early afternoon, the cloud cover remains relatively constant at around 85 % (Figure 3b), while the frequency and intensity of rainfall reaches its peak around 14 UTC (Figure 4d, e). Closely connected to this increase of precipitation are the absolute values of LWP (Figure 4a) as well as the standard deviations of LWP and IWV over one hour (Figure 4b, c). This higher hourly variability of LWP and IWV is associated with the peak of more turbulent convective motions during noon and early afternoon. The increasing precipitation also seems to slightly reduce the number of flying insects (Figure 4d), which recovers after the rain decreases in late afternoon. This is in contrast to the aerosols, whose frequency remains lower after the peak in precipitation has been reached.

In the late afternoon (16–18 UTC), we find in accordance with an assumed slow-down of convective activity the cloud cover to strongly decrease (Figure 3b) as well as the variability of LWP (Figure 4c) and precipitation rate (Figure 4e). The average cloud top and bottom heights (Figure 3c) are increasing in the late afternoon after a steady decrease starting in the morning. This pattern can be understood considering that the derived cloud boundaries represent an average over high and low clouds as well as multi-layer clouds. If we look at the low cloud base frequency (Figure 3d), we can understand this feature: The increasing altitudes of cloud boundaries in the late afternoon seems to be the effect of the decreasing number of low clouds (Figure 3d) and at the same time presence of high ice clouds which might be remnants of convective clouds that developed during the day.

4 Precipitation statistics

In this section, we investigate statistics of daily accumulations of rain and snow derived by two completely different methods. The rain and snowfall amounts derived with the MRR2 are compared to daily accumulated precipitation measurements provided by the DWD weather observer at the summit[2]. The weather observer measures the daily accumulated liquid equivalent snowfall amount at the weather observing platform at 6 UTC. In order to lower potential wind effects on the measurements, the observations at summit are compared to the values measured at the 300 m lower Zugspitzplatt by the Bavarian avalanche warning service. If the measured differences are too large or if wind speeds are very high, the values from the Zugspitzplatt are used (personal communication Manfred Kristen, DWD weather observer Zugspitze).

4.1 Comparison of daily accumulated precipitation derived with MRR to manual observations at summit

We integrated the radar derived rainfall rate and liquid equivalent snowfall rate over 24 h starting at 6 UTC in

[2]https://opendata.dwd.de/climate_environment/CDC/observations_germany/climate/daily/kl/

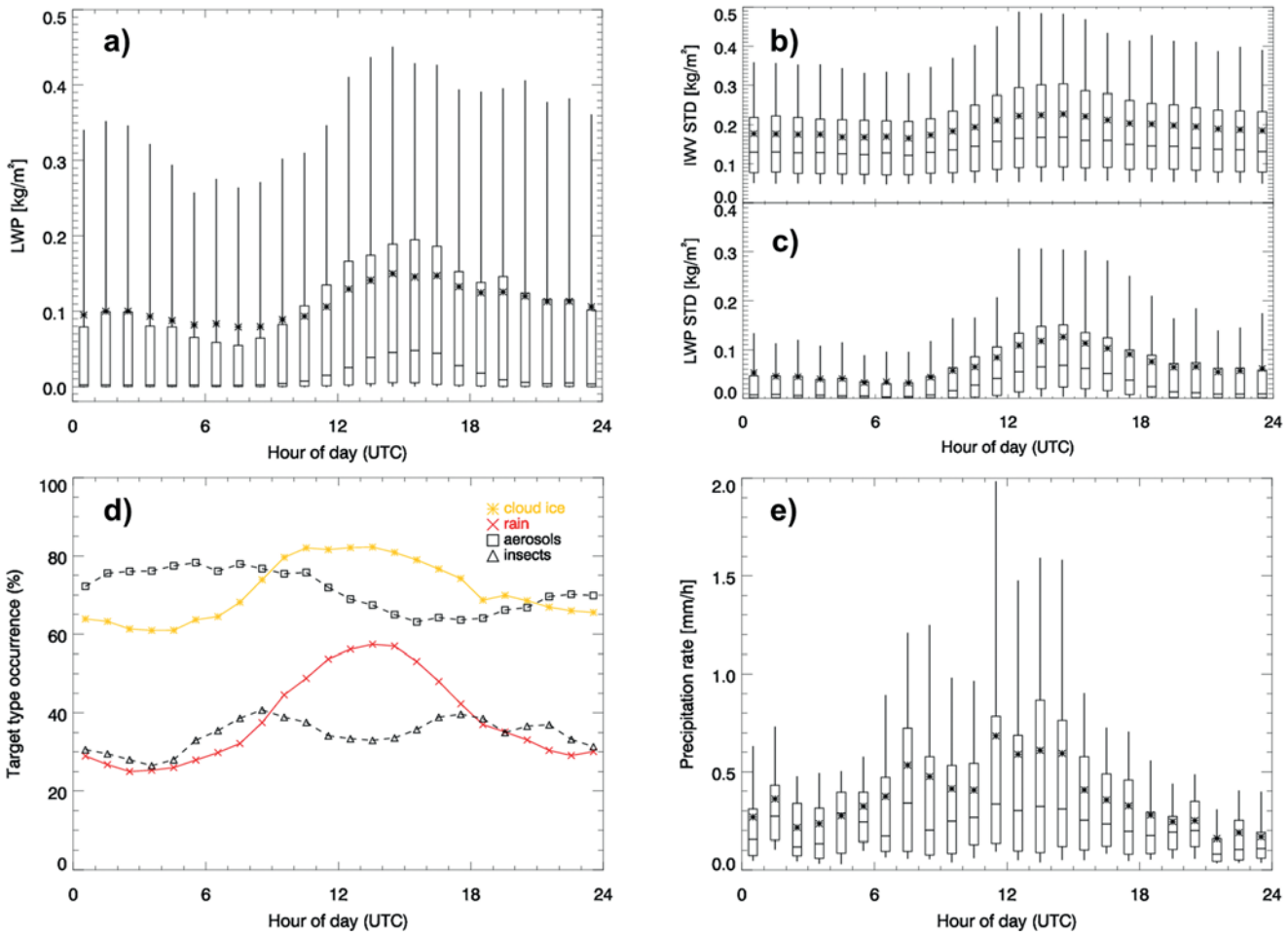

Figure 4: Average diurnal cycle during summer (JJA) of a) LWP, standard deviations of b) IWV and c) LWP, d) occurrence frequency of different Cloudnet classes, and e) precipitation rate. In a)–c), and e) the monthly mean is shown as asterisk, the median is plotted as line inside the box of the 25th and 75th percentile. The whiskers denote the 10th and 90th percentiles.

order to obtain daily precipitation accumulations, which we can directly compare to the weather observer data. Days during which the MRR2 showed data gaps longer than 4 h were discarded from the analysis. Based on our temperature criterion to classify the MRR2 measurements as snowfall or rainfall, we also classify the daily accumulations into rain-only, snow-only, and mixed precipitation events. MRR2 data during mixed precipitation events (i.e. temperatures between −2 and 2 °C) are not used for the following analysis as they might be likely contaminated by melting snow. However, we separately analyze the DWD accumulations for those mixed precipitation events in order to be able to quantify their frequency and relevance for the accumulated precipitation at the UFS.

Figure 5 shows the daily accumulations for snowfall and rainfall days for the three years time period available from MRR2. For snowfall, we find a surprisingly good correlation coefficient of 0.84 and a relatively small bias of 0.07 mm, although large deviations can be found for specific events (Root Mean Square Error RMSE of 6 mm). For rainfall, the correlation coefficient of 0.63 is smaller than for snow, although the bias of 0.12 mm is still very small (RMSE of 5 mm). The much larger scatter for stronger rain events can be partly explained by the fact that nearly all rainfall cases at UFS occur during summer (Figure 1e, f) and many of them are connected to convection. These convective rain events can be intense in terms of RR but also are likely spatially inhomogeneous.

The mostly convective rain showers during summer often produce only small daily accumulations of less than 10 mm (Figure 6a). In comparison, the occurrence frequencies of daily accumulated snowfall are consistently larger than the liquid precipitation with most values populating the range below 30 mm. Again, the distribution of daily precipitation amounts derived from MRR2 and from the DWD are quite similar.

From a hydrological and climatological point of view it is interesting to analyze whether heavy or weak precipitation events contribute more to the long-term accumulated precipitation at the UFS. For this, the total accumulated snow and rain over the entire three years time period is plotted as a function of daily accumulation in

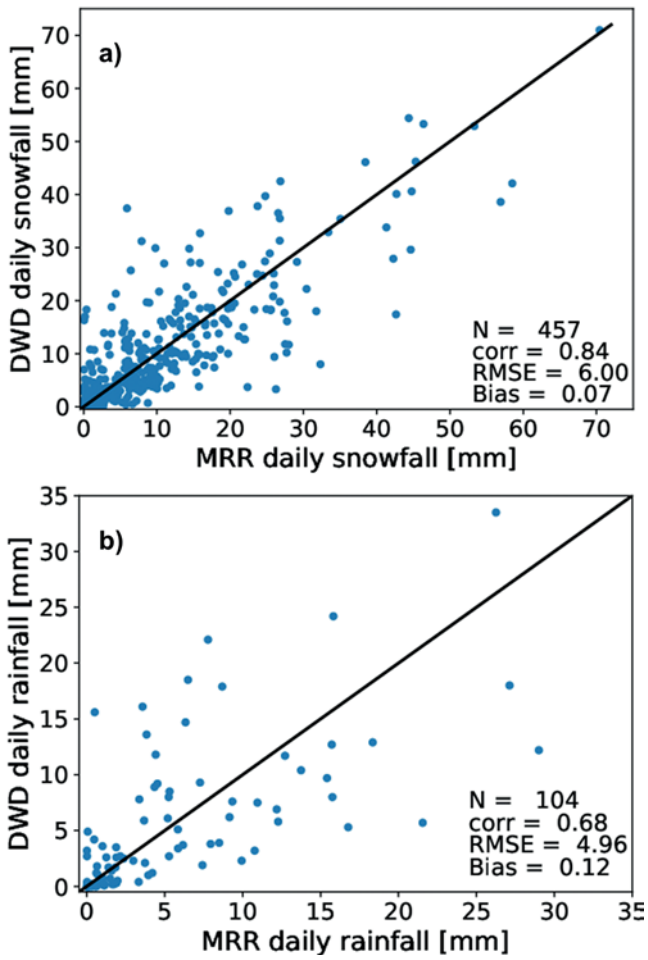

Figure 5: Daily accumulations of a) snowfall (liquid equivalent) and b) rainfall reported by the DWD weather observer and derived from the MRR2 at summit level for the available time periods between September 2012 and August 2015 (for details see text).

Figure 6b. We find a very good agreement with differences of less than 1.4 % for snow and less than 5.5 % for rain compared to the DWD values. In particular, the MRR2 seems to be able to derive both weak and strong precipitation events on average similarly well which was not necessarily expected given that the MRR2 sensitivity is relatively low (ca. −5 dBz compared to typically −50 dBz for a cloud radar) resulting in a limited sensitivity for light rain.

For snowfall, small to medium daily accumulations up to 16 mm contribute already 50 % of the total 3-year accumulation of 4059 mm. If we assume an average snow density of 100 g m^{-3}, these liquid equivalent snow accumulations represent typical daily increases of snow height of up to 16 cm. For rainfall, daily accumulations up to 9 mm are causing 50 % of the total 3-year accumulated rain of 477 mm. This analysis points to the fact, that, on average, snowfall events at UFS are in general more intense than rainfall events and are expectedly the predominant type of precipitation at UFS.

Although, the MRR2 and DWD daily accumulations agree very well, for the complete years of 2013 and 2014 we find the yearly accumulations with 1892 mm and 1708 mm to be smaller than the 2000–2100 mm which we typically would expect from the climatology in this region (Isotta et al., 2014; Wastl and Zängl, 2008). One reason for this difference could be due to year-to-year fluctuations in accumulated precipitation. However, if we integrate the DWD values for the entire year without excluding the MRR2 data gaps, we obtain 1905 mm and 1970 mm for 2013 and 2014, respectively. A closer look into our dataset revealed that for example a ten days data gap (20–30 November 2014) in the MRR2 datasets is responsible for missing 100 mm of precipitation. This result demonstrates, that even short data gaps (MRR2 data availability of 90.6 %) might cause substantial biases for accumulated precipitation estimates.

Overall, rainfall contributes only 10.5 % to the total three years accumulation of 4536 mm. However, if we look into the seasonal distribution of snow, rain, and mixed precipitation (Figure 7), we find the rain to be an important and sometimes even dominant contributor during summer. The largest snow accumulations are found in winter and spring. Although mixed precipitation can contribute significantly to summer accumulation (e.g., summer 2014), the contribution is less than 10 % on average. As an estimation of the amount of mixed-precipitation is currently not possible using the MRR2, the best solution might be to complement the MRR2 observations during summer and autumn with disdrometer observations.

4.2 Occurrence of super-cooled liquid water during snowfall

The multi-year observations at UFS combining a variety of remote sensors gives us the opportunity to explore some of the synergistic information in this dataset. Previous studies of snowfall in mountainous regions (Löhnert et al., 2011; Grazioli et al., 2015) reported the frequent occurrence of SLW during snowfall events. The generation processes of SLW can be manifold, but it is likely that dynamical effects such as turbulence or rapid lifting of air masses, are mainly responsible for the existence of SLW. With our multi-year dataset, we are able to investigate how frequent and how much SLW is contained in clouds which produce snowfall at UFS.

In order to investigate this question, we use the LWP retrieved from HATPRO. Due to HATPRO's heated blower system, it is possible to retrieve LWP even during intense snowfall. For better comparison with the MRR2 and DWD data, the LWP is also averaged to a five minute temporal resolution. All snowfall cases are sorted into different LWP classes (Figure 8a). Consistently with Section 3, LWP values below 10 g m^{-2} are considered to be liquid-free. Only 11.3 % of all snowfall events fall within this category and can be considered to be "dry snowfall". In other words, 88.7 % of all clouds, which produce snowfall at UFS, contain substantial amounts of SLW. The most typical LWP values

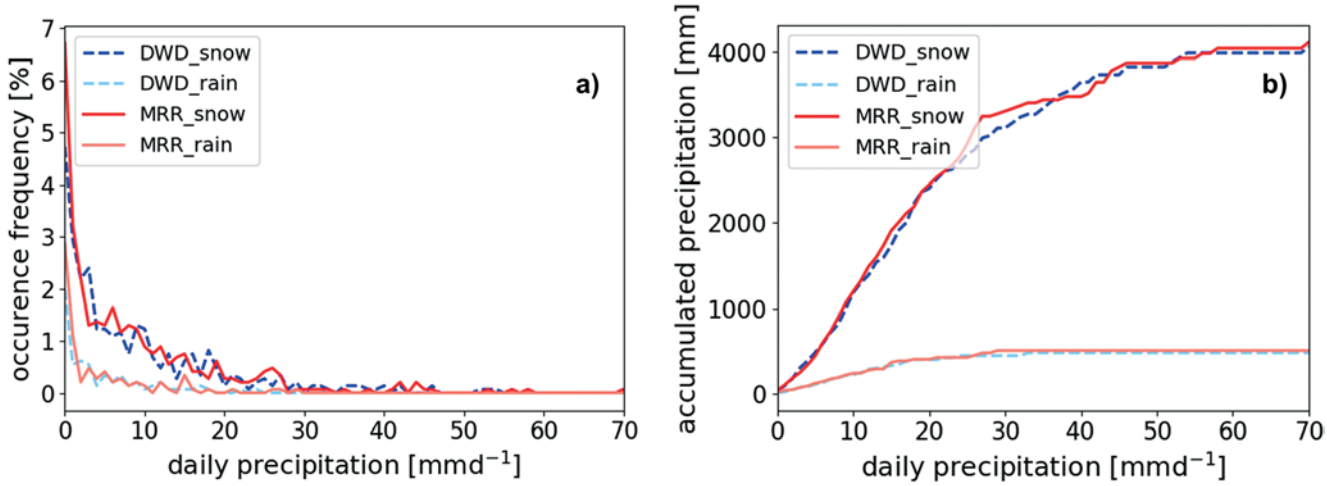

Figure 6: a) Occurrence frequency and b) cumulative amount of daily rainfall and snowfall amounts between Sep. 2012 and Aug. 2015 reported by the DWD weather observer (dashed lines) and derived from MRR2 data (solid lines). The occurrence frequency in a) is normalized with the total number of days.

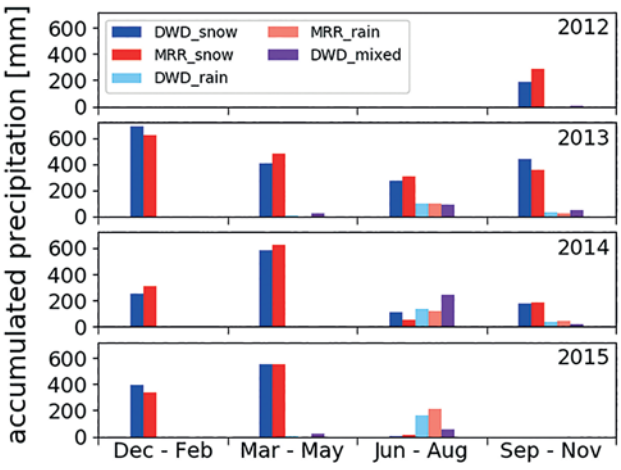

Figure 7: Seasonal amount of snow, rain and mixed precipitation from DWD weather observer reports and derived from MRR2 measurements for different years. Note that no precipitation rate can be derived from MRR2 data for melting snowfall or mixed rain-snow conditions.

during snowfall are found between 30 and 300 g m^{-2}. Only 6.5 % of all snowfall events showed LWP larger than 500 g m^{-2}.

It has been reported by Grazioli et al. (2015) that the snow accumulation is correlated with the amount of riming, i.e., the amount of SLW frozen on the ice and snow particles. Although we have no direct information about the degree of riming for our dataset, we can relate the LWP and the radar derived SR (Figure 8b). There seems to be only a slight tendency of the SR to increase with larger LWP. From the current dataset it is, however, difficult to conclude whether the SLW causes the snow to be more rimed or whether intense snowfall events are caused by strong orographic lifting, which also produces more SLW.

5 Summary

In this study, we investigated a multi-year dataset of clouds and precipitation observed with a combination of microwave radiometer, radar, and ceilometer at the Environmental Research Station Schneefernerhaus (UFS) in the German Alps. While several decade long datasets with this set of remote sensing instruments exist for low elevations, the presented dataset is unique with respect to its time coverage and altitude level.

In the first part of the study, we analyzed the annual and diurnal cycle of various cloud and precipitation variables including vertically integrated water vapor (IWV), liquid water path (LWP), frequency of ice clouds, cloud liquid, rainfall and snowfall rate. In addition, the Cloudnet categorization also provided profiles of the presence of insects and aerosols. The combined observations revealed that clouds and precipitation during summer and winter season are generated by different mechanisms. For the winter months, we are unable to find distinct diurnal cycles in any variables. In agreement with previous studies, which studied the predominant synoptic regimes for different seasons at the UFS, we can explain this absence of diurnal cycles with the predominance of large-scale advection of clouds and precipitation. The diurnal cycles become detectable during warmer months and reach their maximum during summer. Several variables indicate that solar driven thermal motions amplified by the mountain slopes transport air from the lower and more polluted mixed layer in the surrounding valleys up to the level of UFS. This coupling can be most prominently seen in daily IWV anomalies, which reach amplitudes of nearly ±10 kg m^{-2} during summer. These effects also manifests themselves in a diurnal cycle of the presence and vertical extent of aerosols and insects.

The thermally driven transport of moist air also impacts the properties of cloud parameters. During sum-

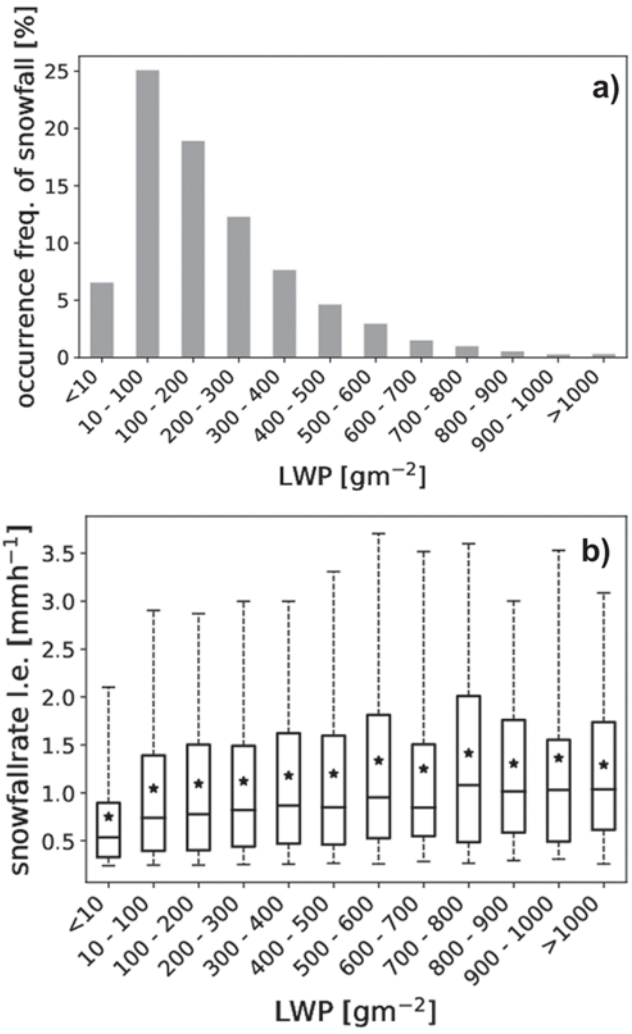

Figure 8: Analysis of the simultaneous occurrence of snowfall derived with MRR2 and super-cooled LWP retrieved with HATPRO in the vertical column above UFS. a) Relative frequency of snowfall of any intensity for different LWP bins. b) Relation of (liquid equivalent) snowfall rate and and LWP. The mean is shown as asterisk, the median is plotted as line inside the box of the 25th and 75th percentile. The whiskers denote the 5th and 95th percentiles.

mer, the mean and extreme values of LWP are found to be almost a factor of two larger as compared to winter. In addition, the LWP also reveals a clear diurnal cycle during summer with a maximum in early afternoon coinciding with the maximum in IWV and frequency of rainfall. Combining these different parameters leads to the conclusion that the clouds and associated precipitation during summer are dominated by convective clouds. The rainfall from these convective clouds is found to be the main contributor to summer precipitation accumulations.

To investigate the seasonal variability of precipitation, we derived rainfall and snowfall rates from MRR radar reflectivities at 300 m range; surface temperature at UFS has been used to separate snowfall and rainfall events. The derived daily accumulations for a three years time period have been compared to the manually recorded precipitation accumulations at the Zugspitze summit by the German Weather Service. Considering the challenges connected with measuring precipitation in a mountainous environment with remote sensors as well as in-situ, the high agreement of the accumulated precipitation, both in rain and snow, are remarkable. Although large deviations are found for single days, the comparison of all daily events shows remarkably small biases, which result in only a 1.4 (5.5) % difference in the total snow (rain) accumulations for the three years period to the weather observer records. These results indicate that it is in principal possible to reliably retrieve daily accumulated precipitation of snow and rain from small and cost-effective radars.

At UFS, 50 % of all daily accumulations are caused by snowfall with daily accumulations up to 16 mm (liquid equivalent) and less than 9 mm for rain. Overall, rainfall contributes only 10.5 % to total precipitation but with strong seasonal dependence. Especially in July, almost all precipitation is falling at UFS as rain. Mixed-phase precipitation can so far not be retrieved from the MRR observations. While mixed-phase precipitation can contribute significant amounts of precipitation during summer, the overall contribution to annual precipitation is less than 10 %. The MRR has been found to be able to derive weak and strong precipitation events at UFS similarly well when compared to the weather observations. When monitoring precipitation with an MRR on a long-term basis, special attention should be paid to avoiding data gaps in the dataset. Although we achieved a 90.6 % data availability of the MRR, a ten days down time in November 2014 was found to be responsible for missing 100 mm precipitation.

Clearly, the strength of the dataset presented in this study lies in the synergy of the various observations. An example presented in this study is the analysis of super-cooled liquid water during snowfall events. We find only 11.3 % of all snowfall events to contain negligible (LWP $< 10\,\mathrm{g\,m^{-2}}$) amounts of LWP. The majority of snowfall events contains LWP values typically ranging between 30 and $300\,\mathrm{g\,m^{-2}}$. Only 6.5 % of all snowfall events showed LWP values exceeding $500\,\mathrm{g\,m^{-2}}$. Although the LWP is expected to play an important role for the microphysical processes in the snow producing clouds, the snowfall rate derived from the MRR is only weakly correlated with the simultaneously measured LWP above the UFS.

The data set offers unique possibilities for evaluating and improving atmospheric models in a mountain environment. Especially, future forecast models approaching the LES (Large Eddy Simulation) scale, explicitly resolving parts of turbulence spectrum and employing high-resolution terrain data, will benefit from such a time series of composite profiling observations. Lastly, the question, if such models actually have the potential of improving forecasts of local, severe weather in a complex mountain environment and orographically induced precipitation enhancement, can only be assessed with such detailed observations as presented in this study.

In addition, the UFS time series offers an anchor point for current and future polar orbiting and geostationary imaging and sounding satellites, such as the MeteoSat Third Generation (MTG). MTG will have severe impact onto European weather observations from space and the observations at UFS can help to evaluate the quality of satellite observations over a high-mountain terrain. Last but not least, the authors are dedicated to keep the remote sensing observations running as long as possible, so that these data can one day serve as a benchmark for the rapidly occurring climate change over the Alps.

Acknowledgments

S. Kneifel acknowledges funding by the the Deutsche Forschungsgemeinschaft (DFG, German Research Foundation) under grant KN 1112/2-1 as part of the Emmy-Noether Group OPTIMIce. L. v. Terzi has been supported by the DFG Priority Program SPP2115 "Fusion of Radar Polarimetry and Numerical Atmospheric Modelling Towards an Improved Understanding of Cloud and Precipitation Processes" (PROM) under grant PROM-IMPRINT (Project Number 408011764). M. Puh and T. Zinner have been supported by DFG SPP2115 PROM grant "IcePolCKa" (project number 408027579, ZI 1132/5-1). We also want to acknowledge the UFS with its shareholders the borough and the county of Garmisch-Partenkirchen, the borough of Grainau and the State of Bavaria. Special thanks go to the UFS staff for their enormous effort to run the station and for the support in maintaining proper operation of the remote sensing instruments. In addition we want to thank Ina Mattis (DWD) and Matthias Wiegner (LMU) for providing the UFS ceilometer data. The Cloudnet project, which is meanwhile part of the ACTRIS (Aerosol, Clouds and Trace Gases Research Infrastructure) Data Centre node for cloud profiling, provided the Cloudnet processing tools. In this respect special thanks go to Ewan O'Connor and Simo Tukiainen of the Finnish Meteorological Institute for their help in setting up the Cloudnet processing and the German HD(CP)^2 (High definition clouds and precipitation for advancing climate prediction) project for facilitating this activity.

A Appendix 1

Estimation of rainfall rate from MRR

Intense rainfall can attenuate the radar signal at 24 GHz even for the relatively short path length of 300 m. Matrosov (2005) shows that at Ka-band the attenuation (α) due to rain can be up to 2.7 dB km^{-1} for a rain rate RR of 10 mm h^{-1} (similar values have been found for K-band by Peters et al., 2010). The attenuation for a given (unattenuated) reflectivity Ze can be derived with a power law $\alpha = a \cdot Ze^b$. The attenuation coefficient α is calculated in units of dB km^{-1} given Ze in linear units of mm^6 m^{-3} with the fit coefficients $a = 0.00205$ and $b = 0.82$. The original fit has been derived by Matrosov (2005) for Ka-band. We tested the difference of attenuation at Ka and K-band assuming a range of rain drop size distributions and found the impact of the frequency difference to be negligible. For the attenuation correction, we assumed the rain DSD to be constant throughout the 300 m layer. It should be noted that rain attenuation within this relatively narrow layer is only relevant for very large reflectivities. Even at a Ze of 30 dBZ, the two-way attenuation for a 300 m layer is calculated to be only 0.35 dB. After attenuation correction, we apply the Ze-RR relation $Ze = 129 \cdot RR^{1.5}$, which has been recently derived for MRRs based on a large set of rainfall events and in-situ observations (Tokay et al., 2009). When inserting Ze in linear units (mm^6 m^{-3}), the RR in units mm h^{-1} can be calculated.

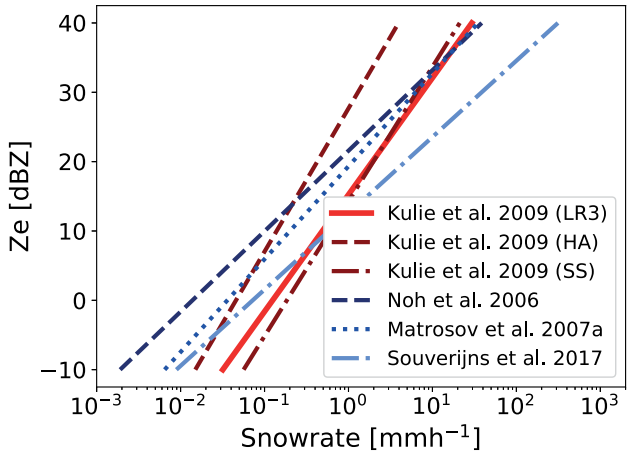

Figure 9: Comparison of different Ze-SR relations from the literature. The LR3 relation from Kulie and Bennartz (2009) was used to calculate the snowfall rate from the MRR2 measurements. Kulie and Bennartz (2009); Matrosov (2007a) are Ze-SR relations for 35.5 GHz, Souverijns et al. (2017) for 24 GHz. To compare the relationships, the Ze(35.5GHZ) were converted to equivalent Ze(24GHz) using the relation from Kneifel et al. (2011a).

Estimation of snowfall rate from MRR

Numerous relations between Ze and snowfall rate (SR) have been published during recent years for various radar frequencies (Figure 9). While for rainfall the particle size distribution (PSD) is the main source of uncertainty, in the case of snowfall, the particles also comprise different mass-size and velocity-size relations, which are closely linked to the particle structure (see Souverijns et al. (2017) for a thorough discussion of the various uncertainties of Ze-SR relations). The structural particle properties are also affecting the scattering properties, although this aspect is less problematic at K-band as compared to W-band (Kneifel et al., 2011a).

Ideally, a Ze-SR relation should be derived from a long-term dataset of collocated in-situ and radar observations (Souverijns et al., 2017). At UFS, we do not

have a suitable in-situ dataset available and the often very windy conditions along the steep mountain slopes makes proper in-situ observations (e.g., PSD, shape, degree of riming) challenging. For this study, we rather chose a Ze-SR relation, which has been derived to estimate global snowfall rate from satellite observation (Kulie and Bennartz, 2009). The "LR3" relation used in Kulie and Bennartz (2009) shows large SR at low Ze but is similar to other Ze-SR relations (Noh et al., 2006; Matrosov, 2007a) at higher Ze (Figure 9). The high SR predicted by the LR3 relation at low Ze fits to observations at UFS here we find very often large amounts of snowfall originating from 1–2 km deep clouds with Ze values lower than 10 dBz. It is, however, clear that selecting a different Ze-SR relation can lead to large deviations in the retrieved total accumulated snow as shown, for example, in Kneifel et al. (2011a) for UFS.

In order to be able to compare the "LR3" retrievals (valid for 35.5 GHz) to MRR2 observations, following the approach in Kneifel et al. (2011a), we first convert Ze at 24 GHz to 35 GHz equivalent Ze and then apply the LR3 Ze-SR relationship ($Z = 24.04 \cdot SR^{1.51}$). No attenuation correction has been applied for snow because attenuation due to ice and snow is usually negligible at Ka- and K-band (Matrosov, 2007b).

Both Ze-RR and Ze-SR relations are usually derived for observations close to sea level pressure. At a higher altitude z, the air density will be lower and thus the terminal fall velocity $v_t(z)$ will increase. We applied the air density correction as described in Heymsfield et al. (2013).

$$v_t(z) = v_t(z)\left(\frac{p(z)}{1013\,\mathrm{hPa}}\right)^{0.4}. \qquad \text{(A.1)}$$

We assume an average atmospheric pressure at the UFS of 730 hPa. Using this value for the pressure $p(z)$ in Eq. (6.1), we find the average terminal velocities to be enhanced by 10 %. This value is in close agreement with the PARSIVEL measurements during rainfall. The increased terminal velocity leads also to a larger RR or SR when assuming an identical PSD. Therefore, we scaled up the radar derived RR and SR by 10 %.

References

Adler, B., N. Kalthoff, M. Kohler, J. Handwerker, A. Wieser, U. Corsmeier, C. Kottmeier, D. Lambert, O. Bock, 2016: The variability of water vapour and pre-convective conditions over the mountainous island of Corsica. – Quart. J. Roy. Meteor. Soc. **142**, 335–346, DOI: 10.1002/qj.2545.

Bollmeyer, C., J.D. Keller, C. Ohlwein, S. Wahl, S. Crewell, P. Friederichs, A. Hense, J. Keune, S. Kneifel, I. Pscheidt, S. Redl, S. Steinke, 2015: Towards a high-resolution regional reanalysis for the european cordex domain. – Quart. J. Roy. Meteor. Soc. **141**, 1–15, DOI: 10.1002/qj.2486.

Carslaw, K.S., M. Wirth, A. Tsias, B.P. Luo, A. Dörnbrack, M. Leutbecher, H. Volkert, W. Renger, J.T. Bacmeister, T. Peter, 1998: Particle microphysics and chemistry in remotely observed mountain polar stratospheric clouds. – J. Geophys. Res. **103**, 5785–5796, DOI: 10.1029/97JD03626.

Delanoë, J., R.J. Hogan, 2010: Combined cloudsat-calipso-modis retrievals of the properties of ice clouds. – J. Geophys. Res. **115**, published online, DOI: 10.1029/2009JD012346.

Dias Neto, J., S. Kneifel, D. Ori, S. Trömel, J. Handwerker, B. Bohn, N. Hermes, K. Mühlbauer, M. Lenefer, C. Simmer, 2019: The triple-frequency and polarimetric radar experiment for improving process observations of winter precipitation. – Earth Sys. Sci. Data **11**, 845–863, DOI: 10.5194/essd-11-845-2019.

Diedrich, H., F. Wittchen, R. Preusker, J. Fischer, 2016: Representativeness of total column water vapour retrievals from instruments on polar orbiting satellites. – Atmos. Chem. Phys. **16**, 8331–8339, DOI: 10.5194/acp-16-8331-2016.

Dmowska, R., J.R. Holton, 1992: Chapter 12 the influence of mountains on airflow, clouds, and precipitation. – In: Cotton, W.R., R.A. Anthes (Eds.): Storm and Cloud Dynamics. – Int. Geophys. **44**, Academic Press, 788–870, DOI: 10.1016/S0074-6142(08)60551-3.

Durán-Alarcón, C., B. Boudevillain, C. Genthon, J. Grazioli, N. Souverijns, N.P.M. van Lipzig, I.V. Gorodetskaya, A. Berne, 2019: The vertical structure of precipitation at two stations in east antarctica derived from micro rain radars. – The Cryosphere **13**, 247–264, DOI: 10.5194/tc-13-247-2019.

Germann, U., G. Galli, M. Boscacci, M. Bolliger, 2006: Radar precipitation measurement in a mountainous region. – Quart. J. Roy. Meteor. Soc. **132**, 1669–1692, DOI: 10.1256/qj.05.190.

Görsdorf, U., V. Lehmann, M. Bauer-Pfundstein, G. Peters, D. Vavriv, V. Vinogradov, V. Volkov, 2015: A 35-ghz polarimetric doppler radar for long-term observations of cloud parameters – description of system and data processing. – J. Atmos. Ocean. Technol. **32**, 675–690, DOI: 10.1175/JTECH-D-14-00066.1.

Grazioli, J., G. Lloyd, L. Panziera, C.R. Hoyle, P.J. Connolly, J. Henneberger, A. Berne, 2015: Polarimetric radar and in situ observations of riming and snowfall microphysics during clace 2014. – Atmos. Chem. Phys. **15**, 13787–13802, DOI: 10.5194/acp-15-13787-2015.

Haeffelin, M., S. Crewell, A.J. Illingworth, G. Pappalardo, H. Russchenberg, M. Chiriaco, K. Ebell, R.J. Hogan, F. Madonna, 2016: Parallel developments and formal collaboration between european atmospheric profiling observatories and the us arm research program. – Meteor. Monographs **57**, 29–1.

Heese, B., H. Flentje, D. Althausen, A. Ansmann, S. Frey, 2010: Ceilometer lidar comparison: backscatter coefficient retrieval and signal-to-noise ratio determination. – Atmos. Meas. Tech. **3**, 1763–1770, DOI: 10.5194/amt-3-1763-2010.

Heymsfield, A.J., C. Schmitt, A. Bansemer, 2013: Ice cloud particle size distributions and pressure-dependent terminal velocities from in situ observations at temperatures from 0° to −86 °C. – J. Atmos. Sci. **70**, 4123–4154, DOI: 10.1175/JAS-D-12-0124.1.

Houze Jr., R.A., 2012: Orographic effects on precipitating clouds. – Rev. Geophys. **50**, published online, DOI: 10.1029/2011RG000365.

Illingworth, A.J., R.J. Hogan, E. O'Connor, D. Bouniol, M.E. Brooks, J. Delanoé, D.P. Donovan, J.D. Eastment, N. Gaussiat, J.W.F. Goddard, M. Haeffelin, H.K. Baltink, O.A. Krasnov, J. Pelon, J.M. Piriou, A. Protat, H.W.J. Russchenberg, A. Seifert, A.M. Tomp-

kins, G.J. van Zadelhoff, F. Vinit, U. Willén, D.R. Wilson, C.L. Wrench, 2007: Cloudnet. – Bull. Amer. Meteor. Soc. **88**, 883–898, DOI: 10.1175/BAMS-88-6-883.

Isotta, F.A., C. Frei, V. Weilguni, M. Percec Tadic, P. Lassegues, B. Rudolf, V. Pavan, C. Cacciamani, G. Antolini, S.M. Ratto, M. Munari, S. Micheletti, V. Bonati, C. Lussana, C. Ronchi, E. Panettieri, G. Marigo, G. Vertacnik, 2014: The climate of daily precipitation in the alps: development and analysis of a high-resolution grid dataset from pan-alpine rain-gauge data. – Int. J. Climatol. **34**, 1657–1675, DOI: 10.1002/joc.3794.

Kästner, M., K. Kriebel, 2001: Alpine cloud climatology using long-term NOAA-AVHRR satellite data. – Theor. Appl. Climatol. **68**, 175–195, DOI: 10.1007/s007040170044.

Kneifel, S., M. Maahn, G. Peters, C. Simmer, 2011a: Observation of snowfall with a low-power FM-CW K-band radar (micro rain radar). – Meteor. Atmos. Phys. **113**, 75–87, DOI: 10.1007/s00703-011-0142-z.

Kneifel, S., M.S. Kulie, R. Bennartz, 2011b: A triple-frequency approach to retrieve microphysical snowfall parameters. – J. Geophys. Res. Atmos. **116**, D11203, DOI: 10.1029/2010JD015430.

Kneifel, S., S. Redl, E. Orlandi, U. Löhnert, M.P. Cadeddu, D.D. Turner, M.T. Chen, 2014: Absorption properties of supercooled liquid water between 31 and 225 GHz: Evaluation of absorption models using ground-based observations. – J. Appl. Meteor. Climatol. **53**, 1028–1045, DOI: 10.1175/JAMC-D-13-0214.1.

Kulie, M.S., R. Bennartz, 2009: Utilizing spaceborne radars to retrieve dry snowfall. – J. Appl. Meteor. Climatol. **48**, 2564–2580.

Löffler-Mang, M., J. Joss, 2000: An optical disdrometer for measuring size and velocity of hydrometeors. – J. Atmos. Ocean. Technol. **17**, 130–139, DOI: 10.1175/1520-0426(2000)017<0130:AODFMS>2.0.CO;2.

Lohmann, U., D. Neubauer, 2018: The importance of mixed-phase and ice clouds for climate sensitivity in the global aerosol–climate model echam6-ham2. – Atmos. Chem. Phys. **18**, 8807–8828, DOI: 10.5194/acp-18-8807-2018.

Löhnert, U., S. Crewell, 2003: Accuracy of cloud liquid water path from ground-based microwave radiometry 1. dependency on cloud model statistics. – Radio Sci. **38**, published online, DOI: 10.1029/2002RS002654.

Löhnert, U., S. Kneifel, A. Battaglia, M. Hagen, L. Hirsch, S. Crewell, 2011: A multisensor approach toward a better understanding of snowfall microphysics: The tosca project. – Bull. Amer. Meteor. Soc. **92**, 613–628, DOI: 10.1175/2010BAMS2909.1.

Löhnert, U., J.H. Schween, C. Acquistapace, K. Ebell, M. Maahn, M. Barrera-Verdejo, A. Hirsikko, B. Bohn, A. Knaps, E. O'Connor, C. Simmer, A. Wahner, S. Crewell, 2015: Joyce: Jülich observatory for cloud evolution. – Bull. Amer. Meteor. Soc. **96**, 1157–1174, DOI: 10.1175/BAMS-D-14-00105.1.

Lonitz, K., A.J. Geer, 2019: Assessing the impact of different liquid water permittivity models on the fit between model and observations. – Atmos. Meas. Tech. **12**, 405–429, DOI: 10.5194/amt-12-405-2019.

Lüdecke, C., 2000: Hundert Jahre meteorologische Hochstation auf der Zugspitze – Der Deutsch-österreichische Alpenverein als Förderer der alpinen Meteorologie. – Meteorol. Z. **9**, 381–391, DOI: 10.1127/metz/9/2000/381.

Lugauer, M., P. Winkler, 2005: Thermal circulation in south bavaria climatology and synoptic aspects. – Meteorol. Z. **14**, 15–30, DOI: 10.1127/0941-2948/2005/0014-0015.

Lundquist, J., M. Hughes, E. Gutmann, S. Kapnick, 2019: Our skill in modeling mountain rain and snow is bypassing the skill of our observational networks. – Bull. Amer. Meteor. Soc. **100**, 2473–2490, DOI: 10.1175/BAMS-D-19-0001.1.

Maahn, M., P. Kollias, 2012: Improved micro rain radar snow measurements using doppler spectra post-processing. – Atmos. Meas. Tech. **5**, 2661–2673, DOI: 10.5194/amt-5-2661-2012.

Maahn, M., C. Burgard, S. Crewell, I.V. Gorodetskaya, S. Kneifel, S. Lhermitte, K. Van Tricht, N.P.M. van Lipzig, 2014: How does the spaceborne radar blind zone affect derived surface snowfall statistics in polar regions? – J. Geophys. Res. **119**, 604–620, DOI: 10.1002/2014JD022079.

Marchand, R., G.G. Mace, A.G. Hallar, I.B. McCubbin, S.Y. Matrosov, M.D. Shupe, 2013: Enhanced radar backscattering due to oriented ice particles at 95 GHz during stormvex. – J. Atmos. Ocean. Technol. **30**, 2336–2351, DOI: 10.1175/JTECH-D-13-00005.1.

Marke, T., K. Ebell, U. Löhnert, D.D. Turner, 2016: Statistical retrieval of thin liquid cloud microphysical properties using ground-based infrared and microwave observations. – J. Geophys. Res. **121**, 558–573, DOI: 10.1002/2016JD025667.

Matrosov, S.Y., 2005: Attenuation-based estimates of rainfall rates aloft with vertically pointing ka-band radars. – J. Atmos. Ocean. Technol. **22**, 43–54, DOI: 10.1175/JTECH-1677.1.

Matrosov, S.Y., 2007a: Modeling backscatter properties of snowfall at millimeter wavelengths. – J. Atmos. Sci. **64**, 1727–1736.

Matrosov, S.Y., 2007b: Modeling backscatter properties of snowfall at millimeter wavelengths. – J. Atmos. Sci. **64**, 1727–1736, DOI: 10.1175/JAS3904.1.

Myagkov, A., S. Kneifel, T. Rose, 2020: Evaluation of the reflectivity calibration of W-band radars based on observations in rain. – Atmos. Meas. Tech. **13**, 5799–5825, DOI: 10.5194/amt-13-5799-2020.

Napoli, A., A. Crespi, F. Ragone, M. Maugeri, C. Pasquero, 2019: Variability of orographic enhancement of precipitation in the alpine region. – Sci. Reports **9**, 2045–2322, DOI: 10.1038/s41598-019-49974-5.

Noh, Y.J., G. Liu, E.K. Seo, J.R. Wang, K. Aonashi, 2006: Development of a snowfall retrieval algorithm at high microwave frequencies. – J. Geophys. Res. **111**, published online, DOI: 10.1029/2005JD006826.

Peters, G., B. Fischer, T. Andersson, 2002: Rain observations with a vertically looking micro rain radar (mrr). – Boreal Env. Res. **7**, 353–362.

Peters, G., B. Fischer, M. Clemens, 2010: Rain Attenuation of Radar Echoes Considering Finite-Range Resolution and Using Drop Size Distributions. – J. Atmos. Ocean. Technol. **27**, 829–842, DOI: 10.1175/2009JTECHA1342.1.

Protat, A., A. Armstrong, M. Haeffelin, Y. Morille, J. Pelon, J. Delanoë, D. Bouniol, 2006: Impact of conditional sampling and instrumental limitations on the statistics of cloud properties derived from cloud radar and lidar at sirta. – Geophys. Res. Lett. **33**, published online, DOI: 10.1029/2005GL025340.

Ramelli, F., J. Henneberger, R.O. David, J. Bühl, M. Radenz, P. Seifert, J. Wieder, A. Lauber, J.T. Pasquier, R. Engelmann, C. Mignani, M. Hervo, U. Lohmann, 2021: Microphysical investigation of the seeder and feeder region of an alpine mixed-phase cloud. – Atmos. Chem. Phys., **21**, 6681–6706, DOI: 10.5194/acp-21-6681-2021.

Risius, S., H. Xu, F. Di Lorenzo, H. Xi, H. Siebert, R.A. Shaw, E. Bodenschatz, 2015: Schneefernerhaus as a mountain research station for clouds and turbulence. – Atmos. Meas. Tech. **8**, 3209–3218, DOI: 10.5194/amt-8-3209-2015.

Rose, T., S. Crewell, U. Löhnert, C. Simmer, 2005: A network suitable microwave radiometer for operational monitoring of the cloudy atmosphere. – Atmos. Res. **75**, 183–200, DOI: 10.1016/j.atmosres.2004.12.005.

Rosenkranz, P.W., 2015: A model for the complex dielectric constant of supercooled liquid water at microwave frequencies. – IEEE Trans. Geosci. Remote Sens. **53**, 1387–1393, DOI: 10.1109/TGRS.2014.2339015.

Rotunno, R., R.A. Houze, 2007: Lessons on orographic precipitation from the mesoscale alpine programme. – Quart. J. Roy. Meteor. Soc. **133**, 811–830, DOI: 10.1002/qj.67.

Schultz, M.G., H. Akimoto, J. Bottenheim, B. Buchmann, I.E. Galbally, S. Gilge, D. Helmig, H. Koide, A.C. Lewis, P.C. Novelli, C. Plass-Dülmer, T.B. Ryerson, M. Steinbacher, R. Steinbrecher, O. Tarasova, K. Tørseth, V. Thouret, C. Zellweger, 2015: The Global Atmosphere Watch reactive gases measurement network. – Elementa: Science of the Anthropocene **3**, 000067, DOI: 10.12952/journal.elementa.000067.

Schween, J.H., J. Kuettner, D. Reinert, J. Reuder, V. Wirth, 2007: Definition of "banner clouds" based on time lapse movies. – Atmos. Chem. Phys. **7**, 2047–2055, DOI: 10.5194/acp-7-2047-2007.

Sigmund, A., K. Freier, T. Rehm, L. Ries, C. Schunk, A. Menzel, C.K. Thomas, 2019: Multivariate statistical air mass classification for the high-alpine observatory at the Zugspitze mountain, Germany. – Atmos. Chem. Phys. **19**, 12477–12494, DOI: 10.5194/acp-19-12477-2019.

Smalley, M., T. L'Ecuyer, M. Lebsock, J. Haynes, 2014: A comparison of precipitation occurrence from the ncep stage iv qpe product and the cloudsat cloud profiling radar. – J. Hydrometeorol. **15**, 444–458, DOI: 10.1175/JHM-D-13-048.1.

Souverijns, N., A. Gossart, S. Lhermitte, I. Gorodetskaya, S. Kneifel, M. Maahn, F. Bliven, N. van Lipzig, 2017: Estimating radar reflectivity – snowfall rate relationships and their uncertainties over antarctica by combining disdrometer and radar observations. – Atmos. Res. **196**, 211–223, DOI: 10.1016/j.atmosres.2017.06.001.

Steinke, S., S. Wahl, S. Crewell, 2019: Benefit of high resolution cosmo reanalysis: The diurnal cycle of column-integrated water vapor over Germany. – Meteorol. Z. **28**, 165–177, DOI: 10.1127/metz/2019/0936.

Stephens, G., D. Winker, J. Pelon, C. Trepte, D. Vane, C. Yuhas, T. L'Ecuyer, M. Lebsock, 2018: Cloudsat and calipso within the a-train: Ten years of actively observing the earth system. – Bull. Amer. Meteor. Soc. **99**, 569–581, DOI: 10.1175/BAMS-D-16-0324.1.

Tokay, A., P. Hartmann, A. Battaglia, K.S. Gage, W.L. Clark, C.R. Williams, 2009: A field study of reflectivity and z–r relations using vertically pointing radars and disdrometers. – J. Atmos. Ocean. Technol. **26**, 1120–1134.

Turner, D., S. Kneifel, M. Cadeddu, 2016: An improved liquid water absorption model at microwave frequencies for supercooled liquid water clouds. – J. Atmos. Ocean. Technol. **33**, 33–44, DOI: 10.1175/JTECH-D-15-0074.1.

Viviroli, D., R. Weingartner, B. Messerli, 2003: Assessing the hydrological significance of the world's mountains. – Mountain Res. Develop. **23**, 32–40.

Wastl, C., G. Zängl, 2007: Analysis of the climatological precipitation gradient between the alpine foreland and the northern alps. – Meteorol. Z. **16**, 541–552, DOI:10.1127/0941-2948/2007/0223.

Wastl, C., G. Zängl, 2008: Analysis of mountain-valley precipitation differences in the alps. – Meteorol. Z. **17**, 311–321, DOI:10.1127/0941-2948/2008/0291.

Wiegner, M., A. Geiss, 2012: Aerosol profiling with the jenoptik ceilometer chm15kx. – Atmos. Meas. Tech. **5**, 1953–1964, DOI: 10.5194/amt-5-1953-2012.

Wirth, V., M. Kristen, M. Leschner, J. Reuder, J.H. Schween, 2012: Banner clouds observed at mount zugspitze. – Atmos. Chem. Phys. **12**, 3611–3625, DOI: 10.5194/acp-12-3611-2012.

Witschas, B., C. Lemmerz, O. Reitebuch, 2012: Horizontal lidar measurements for the proof of spontaneous rayleigh-brillouin scattering in the atmosphere. – Appl. Opt. **51**, 6207–6219, DOI: 10.1364/AO.51.006207.

Wulfmeyer, V., A. Behrendt, C. Kottmeier, U. Corsmeier, C. Barthlott, G.C. Craig, M. Hagen, D. Althausen, F. Aoshima, M. Arpagaus, H.S. Bauer, L. Bennett, A. Blyth, C. Brandau, C. Champollion, S. Crewell, G. Dick, P. Di Girolamo, M. Dorninger, Y. Dufournet, R. Eigenmann, R. Engelmann, C. Flamant, T. Foken, T. Gorgas, M. Grzeschik, J. Handwerker, C. Hauck, H. Höller, W. Junkermann, N. Kalthoff, C. Kiemle, S. Klink, M. König, L. Krauss, C.N. Long, F. Madonna, S. Mobbs, B. Neininger, S. Pal, G. Peters, G. Pigeon, E. Richard, M.W. Rotach, H. Russchenberg, T. Schwitalla, V. Smith, R. Steinacker, J. Trentmann, D.D. Turner, J. van Baelen, S. Vogt, H. Volkert, T. Weckwerth, H. Wernli, A. Wieser, M. Wirth, 2011: The convective and orographically-induced precipitation study (cops): the scientific strategy, the field phase, and research highlights. – Quart. J. Roy. Meteor. Soc. **137**, 3–30, DOI: 10.1002/qj.752.

Xie, X., U. Löhnert, S. Kneifel, S. Crewell, 2012: Snow particle orientation observed by ground-based microwave radiometry. – J. Geophys. Res. **117**, published online, DOI: 10.1029/2011JD016369.

Zängl, G., 2008: The temperature dependence of small-scale orographic precipitation enhancement. – Quart. J. Roy. Meteor. Soc. **134**, 1167–1181, DOI: 10.1002/qj.267.

Zinner, T., P. Hausmann, F. Ewald, L. Bugliaro, C. Emde, B. Mayer, 2016: Ground-based imaging remote sensing of ice clouds: uncertainties caused by sensor, method and atmosphere. – Atmos. Meas. Tech. **9**, 4615–4632, DOI: 10.5194/amt-9-4615-2016.